Characteristics of turbulent square duct flows over porous media

Characteristics of turbulent square duct flows over porous media

Kazuhiko Suga[1]†, Yuki Okazaki[1] and Yusuke Kuwata[1]

[1]Department of Mechanical Engineering, Osaka Prefecture University, Osaka 599-8531, Japan

(Received xx; revised xx; accepted xx)

To assess the fully developed turbulence in square sectioned porous duct flows, particle image velocimetry measurements are carried out. To the bottom duct wall, this study applies two types of porous media whose porosities are approximately 0.8 and ratios of the wall-normal to streamwise permeabilities are 0.8 and 7.8. Both over- and under-surface turbulence of the porous layers are discussed at the inlet flow Reynolds numbers of $Re \simeq$ 3500 and 7500. Cross sectional secondary flows are detected with the enhanced magnitude of approximately 6% of the inlet bulk velocity. The secondary flow pattern consisting of four large vortices is observed to be insensitive to the porous structures. Over the porous wall, although turbulence is enhanced by the permeability, it is confirmed that turbulence over and under the porous surfaces is rather insensitive to the wall-normal permeability compared with the streamwise permeability as seen in porous walled channel flows. In the present range of the streamwise permeability Reynolds number of $Re_{K_x} = 2.49 -$ 6.37, the wall-normal fluctuations become dominant once underneath the porous surface while the streamwise ones become dominant again deep inside the porous layer. Applying the streamwise-spanwise plane averaging, which covers a 52% area in the middle of the duct, to the flow quantities, it is confirmed that the correlations between the pore-scale Reynolds number and the log-law parameters are similar to those seen in a wide range of porous walled channels. The above characteristics are generally the same as those of porous walled channels at the same range of the porosities and the permeability Reynolds numbers even with the enhanced secondary flows. However, from the spectral analysis of flows at the porous walls, it is found that near the symmetry planes, the wavelengths of the Kelvin-Helmholtz waves become a little shorter than those in turbulent porous-wall channels possibly because of the side wall boundary layers particularly at low Reynolds numbers.

Key words:

1. Introduction

Since engineering flow passages are usually ducts or pipes and often bounded by permeable porous surfaces, discussions on turbulent porous duct flows are essential for industrial applications. For example, carbon papers, which are anisotropic porous media, are usually used for gas diffusion layers (GDLs) of proton exchange membrane fuel cells (PEMFCs). As the flow Reynolds number of a rectangular channel (duct) flow over a GDL in a PEMFC often reaches $Re \simeq 3000$ (Suga *et al.* 2014), for designing PEMFCs, it is important to understand turbulence over porous media in a rectangular

† Email address for correspondence: suga@me.osakafu-u.ac.jp

duct. Nevertheless, to the best of the authors' knowledge, there is only a few studies which performed detailed discussions on such a topic in the literature. Among them, the recent particle image velocimetry (PIV) measurements by Kim *et al.* (2018) discussed square duct turbulence over an isotropic porous beds by the refractive-index (RI) matching method with an aqueous solution of sodium iodide (NaI). Their porous beds consisted of acrylic sphere balls with the porosity $\varphi = 0.48$. However, their measurements were for the developing flow region and the flows were not affected by the side walls. The direct numerical simulation (DNS) study for a turbulent porous duct flow by Samanta *et al.* (2015) treated a square duct flow with an isotropic porous bottom wall. They applied the volume averaged Navier-Stokes (VANS) equation to model the flow inside the porous wall assuming that the porosity of the porous medium, the bulk and permeability Reynolds numbers were $\varphi = 0.95$, $Re_b = 5000$ and Re_K =8.9, respectively. The permeability Reynolds number is defined as $Re_K = u_\tau^p \sqrt{K}/\nu$ which is based on the friction velocity u_τ^p on the porous wall, the fluid kinematic viscosity ν and the wall permeability K. Although the flows were affected by the side walls, the obtained general flow trends near the symmetry plane seemed similar to those of the porous wall turbulence in two-dimensional (2D) flow systems such as channels or boundary layers. They were that the flow became more turbulent over the porous wall and the emergence of short spanwise roller vortices, which were generated by a Kelvin-Helmholtz (K-H) type of instability, replaced the streaky wall-bounded turbulence structure. Although these trends followed those of the porous wall turbulence in 2D flow systems, it was uncertain how similar they were. Since they reported that the magnitude of the secondary flow exceeded that of a regular solid duct of Vinuesa *et al.* (2014) by a factor of four, it is important to know whether the secondary flows change the flow characteristics around the porous interface.

As for the porous wall turbulence in 2D flow systems, many researchers including the present authors have reported turbulent flow characteristics (e.g. Lovera & Kennedy 1969; Ruff & Gelhar 1972; Zagni & Smith 1976; Zippe & Graf 1983; Breugem *et al.* 2006; Pokrajac & Manes 2009; Manes *et al.* 2009; Suga *et al.* 2010, 2011, 2017; Manes *et al.* 2011; Suga 2016; Kuwata & Suga 2016*a*). From those studies, what we learnt is that the wall permeability significantly affects turbulence near a wall enhancing momentum exchange. Since vortex flow motions may penetrate into a porous wall, wall blocking effects on turbulence are relaxed resulting in strong wall-normal velocity-fluctuations and thus shear stress at the wall. Most of the above cited studies applied isotropic porous media and hence some of the understandings may lack generality. Correspondingly, to extend our knowledge to cover turbulence over anisotropic porous media, the present authors performed PIV experiments of turbulent flows over orthotropic porous media (Suga *et al.* 2018). Here, orthotropic porous media are kinds of anisotropic porous media whose structures are uniform along the coordinate axes. We suggested that turbulence generation over porous media was relatively insensitive to the wall-normal permeability K_{yy} when the ratio between the wall-normal and streamwise permeabilities is $R_{yx} = K_{yy}/K_{xx} \geqslant 1.0$. Note that the permeability is defined as a second rank tensor as K_{ij} (Whitaker 1986) and in this study its diagonal components K_{xx}, K_{yy} and K_{zz} are simply called streamwise, wall-normal and spanwise permeabilities, respectively. The above suggested trend was supported by our DNS study of Kuwata & Suga (2017). However, for the cases at $R_{yx} < 1.0$, DNS studies of Abderrahaman-Elena & García-Mayoral (2017); Gómez-de Segura *et al.* (2018) suggested that turbulent drag might reduce compared with that over a solid smooth wall when $1/R_{yx}$ was extremely large. Those drag reduction DNS studies considered flows at very low permeability Reynolds numbers of $Re_{K_y} < 1$. This Reynolds number is defined as $Re_{K_\alpha} = u_\tau^p \sqrt{K_{\alpha\alpha}}/\nu$ which is based on $K_{\alpha\alpha}$ ($\alpha = x, y, z$ without summation convention). (For isotropic porous media, the permeability Reynolds number Re_K, which is equivalent to Re_{K_α}, is used since $K = K_{\alpha\alpha}$.) They commented that the K-H instability, which is the main factor to enhance turbulence over permeable surfaces, was not induced at $Re_{K_y} < 1$. Rosti *et al.* (2018) supported this discussion showing the drag reduction at $1/R_{yx} > 16$ while the drag was increased at $R_{yx} > 1.0$. Those results may show us the way to go for devising new drag reducing surfaces. However, the realizability of such drag reducing condition may not be fully convinced since the flows inside porous media of those studies were modelled by the Brinkmann equation (Abderrahaman-Elena & García-Mayoral 2017; Gómez-de Segura *et al.* 2018) or were not solved by using idealized surface boundary conditions (Rosti *et al.* 2018).

Turbulence characteristics under porous surfaces are also important because they affect heat and mass transfer performance across the porous walls. It is considered that such characteristics depend on the structure of porous medium. However, since resolving a porous structure is very cost demanding for numerical simulations, DNS studies such as those by Breugem *et al.* (2006) and Samanta *et al.* (2015) applied the VANS model for the porous media. With the VANS model for a flow inside a porous medium of $\varphi = 0.95$ at $Re_K = 9.35$, Breugem *et al.* (2006) predicted that turbulence immediately became isotropic just underneath the porous interface. On the other hand, another DNS by these authors (Breugem & Boersma 2005) showed different turbulence trend inside a fully resolved porous medium. Their porous medium consisted of a three dimensional Cartesian grid of floating cube blocks whose porosity was $\varphi = 0.875$. At $Re_K = 12.4$, turbulence anisotropy was maintained deep inside the porous medium. The streamwise turbulent intensity was always most dominant inside the porous layer while the wall-normal intensity surpassed the spanwise component. DNS studies by the present authors (Kuwata & Suga 2016*b*, 2017) also resolved porous structures. Kuwata & Suga (2016*b*) applied interconnected staggered cube arrays to construct a porous medium and reported structural dependent turbulence profiles inside the porous layer of $\varphi = 0.71$, at $Re_K = 3.8$. The notable point was that their wall-normal turbulent intensity became most dominant surpassing the streamwise component below one-pore length depth from the porous surface while turbulence became eventually isotropic deep inside the porous layer. In different porous structure which consisted of a three dimensional Cartesian grid of cubic pores of $\varphi = 0.84$, Kuwata & Suga (2017) showed that the wall-normal turbulent intensity at $Re_K = 6.1$ was the most dominant component until one-pore length depth from the surface.

Since the vegetation canopies are kinds of porous media, open-channel flows with submerged vegetation canopies were measured by civil/environmental researchers (e.g. Dunn *et al.* 1996; Nezu & Sanjou 2008). For laser Doppler anemometry (LDA) measurements, Nezu & Sanjou (2008) applied regular arrays of rectangular plates to model the vegetation canopy of $\varphi = 0.985$. Dunn *et al.* (1996) applied staggered circular cylinder arrays of $\varphi = 0.988$ for their three-dimensional acoustic Doppler velocimetry measurements. Although they did not report, the permeability Reynolds numbers estimated by Kuwata & Suga (2015) were $Re_{K_y} \simeq 140$ and 1200 for the cases of Nezu & Sanjou (2008) and Dunn *et al.* (1996), respectively. For both the cases, since the porosities and the permeability Reynolds numbers were extremely high, near surface turbulence anisotropy was maintained inside the canopies. The most dominant turbulent intensity was the streamwise component while the smallest one was the wall-normal component. We thus understand that turbulence anisotropy under the porous surface depends on the Reynolds number and the porous structure if the porosity is relatively high. (Since it is generally difficult to optically access to deep inside the porous media, we do not find so many other detailed experimental reports on turbulence under porous surfaces in the literature.

Although the aforementioned PIV study by Kim *et al.* (2018) also measured turbulence inside isotropic porous medium, they only showed the wall-normal turbulent intensity inside the porous beds.)

Consequently, although our knowledge on porous wall turbulence is not deep enough yet even for 2D flow systems, it is still useful to understand whether we can apply the knowledge to the rectangular porous duct systems. Hence, to assess the turbulence in square sectioned porous duct flows, this study measures both over- and under-surface turbulence of porous layers. The permeability ratios of the present porous media are $R_{yx} = 0.8$ and 7.8. Those anisotropic porous layers are made of acrylic square rods and the porosity of the former case is $\varphi = 0.77$ while that of the latter case is $\varphi = 0.75$. For both the cases, flows at the Reynolds numbers of $Re = U_0H/\nu \simeq 3500$ and 7500 are measured by a planar PIV system. Here, U_0 and H are the inlet mean velocity to the square duct and the duct height, respectively. The corresponding permeability Reynolds number ranges $Re_{K_y} = 2.37-16.20$ which are for enhancing turbulence and mass transfer. Note that the conditions of the DNS studies of Abderrahaman-Elena & García-Mayoral (2017); Gómez-de Segura *et al.* (2018) were very different from those of the present experiments. Their assumption of $Re_{K_y} < 1$ indicated that the scales of the wall-normal permeabilities were smaller than the size of the smallest turbulent eddies. Moreover, because the DNS of Samanta *et al.* (2015) assumed an isotropic porous medium and applied the VANS equation to the flow inside it, anisotropic permeability and structural effects could not be discussed. Therefore, this study discusses the structural effects on porous duct turbulence and tries to confirm whether common features of turbulence over porous media are maintained under enhanced secondary flows.

2. Experimental method

Figure 1 (*a*) illustrates the flow facility and the test section of the present experimental setup. Tap water, whose temperature is maintained by a cooler at 292 ± 1 K, is pumped to a straightener and nozzle section through a digital flow meter (FD-MH200A, KEYENCE) which measured the total flow rate. By a digital thermometer (FD-T1, KEYENCE) settled in the nozzle, the water temperature is recorded. The conditioned flow by the honeycomb-bundled nozzle with turbulence grids at the exit enters to a 3.0 m long duct whose cross section (height×width) is 100×50 mm^2 as shown in figure 1 (*b*). The fully developed flow is measured at 2.7 m from the duct entrance. (See Appendix A for the confirmation of the flow development.) As seen in figure 1 (*b*), the duct consists of solid smooth acrylic walls and a porous layer filled in the bottom half of the duct. The height and width of the clear fluid region are H=50 mm. To maintain the optical access to the porous region, transparent acrylic rods with 3×3 mm^2 square cross sections are used to construct two different porous media: cases A and B, as shown in figure 2 (*a*, *b*). To construct the porous media, the rod pitches in the streamwise and spanwise directions are set to 13 mm forming square pores whose side-length is D = 10 mm. To avoid the surface layer of rods acting as a surface roughness, the porous surfaces are covered with meshes having the same square pores. (We understand that not covering the surfaces by such meshes may be more desirable. However, our experiments of similar flows with rib-roughness (Okazaki *et al.* 2018) found that surface turbulence was more significantly modified by the rib-roughness than the permeability.) As seen in figure 2 (*a*, *b*), the rods are piled up in the staggered manner in the streamwise and spanwise direction for case A, while the rods are piled up in the straight manner for case B. The porosities of the porous media are φ = 0.77 and 0.75 for cases A and B, respectively. The measured permeabilities and Forchheimer coefficients are listed in table 1. The wall-normal diagonal component of the permeability tensor is designed to be different from the other components by the factors of 0.8 and 7.8 for cases A and B, respectively. The diagonal components of the permeability tensor $K_{\alpha\alpha}$ and the Forchheimer tensor $F_{\alpha\alpha}$ are measured using the horizontal duct flow facility. With measured pressure drops $\partial \langle p \rangle^f / \partial x_\alpha$ along the α–axis of the media and several different flow rates, the diagonal components of the permeability and Forchheimer tensors are calculated using the Darcy-Forchheimer equation of Whitaker (1986):

$$\langle u_i \rangle = -\frac{K_{ij}}{\mu} \frac{\partial \langle p \rangle^f}{\partial x_j} - F_{ij} \langle u_j \rangle \,, \tag{2.1}$$

where $\langle u_i \rangle$, $\langle p \rangle^f$ and μ are the superficially volume averaged velocity u_i, the volume averaged fluid-phase pressure and the dynamic viscosity of the fluid, respectively. Note that since the porous media are orthotropic, for measuring the values of each axe we turned the media by arranging the axe of the medium and the flow direction in line. The superscript "f" denotes a value in the fluid-phase. The Forchheimer tensor F_{ij} is modelled as $F_{ij} = \rho C^F_{ij} |\langle \mathbf{u} \rangle| / \mu$, where ρ is the densiy of the fluid. Note that for the material whose structure is symmetric in the x-, y- and z-directions, the permeability and Forchheimer tensors become diagonal.

The present planar PIV system consists of a diode pumped solid state laser (Ray Power 2000, Dantec Dynamics) with the wavelength of 532 nm, a high speed complementary metal-oxide semiconductor (CMOS) camera (Speed Sense 9040, Phantom), a camera lens with a long-pass filter whose cut-off wavelength is 570 nm and a computer for data sampling. For the tracer particles, polymer fluorescent particles containing Rhodamine B, whose mean diameter and specific gravity are respectively 10 mm and 1.50, are used. The seeding density is adjusted to obtain 16 particle images in each interrogation window whose size is set to 32 × 32 pixels. The interrogation windows are overlapped 50% in each direction. The aspect ratio of the high-speed camera frame is 1.36:1 and the frame resolution is 1632×1200 pixels. The laser light sheet is approximately 1.0 mm thickness and illuminates the measuring sections. The streamwise-spanwise (x–z) and streamwise-wall-normal (x–y) plane measurements are performed at $Re = U_0 H/\nu \simeq 3500$ and 7500. Here, the mean inlet velocity U_0 is the mean velocity at the nozzle exit of $H \times H$. For the x–z plane measurements, as shown in figure 2(c), for case B, 13 planes (plane $y1 - y13$) at $y/H = -0.21$, -0.15, -0.09, -0.03, 0.1, 0.2, 0.3, 0.4, 0.5, 0.6, 0.7, 0.8 and 0.9 are measured. For the x–y plane measurements, as shown in figure 2(d), 7 planes (plane $z1 - z7$) at $z/H = 0.0$, 0.065, 0.13, 0.195, 0.26, 0.325 and 0.39 are measured for both cases A and B. Note that the porous interface is at $y/H = 0$ and the spanwise symmetry plane is at $z/H = 0$. To maintain the measuring accuracy inside the porous media, a single measuring section of a x–y plane is divided into two zones: clear flow and porous medium zones, with an overlapping region under the porous surface. For these zones, a single recorded frame of the camera covers 75×55 and 65×48 mm^2, respectively. Thus, the measurement sampling volumes are $1.47(x) \times 1.47(y) \times 1.0(z)$ mm^3 and $1.28(x) \times 1.28(y) \times 1.0(z)$ mm^3, respectively. The trigger rate of the high speed camera is adjusted depending on the averaged particle displacement during the time interval. Hence, the image sampling rate varies in the range of 200 – 500 Hz. The averaged particle displacement is set to be 25% length (8 pixels) of the interrogation window cell. To obtain the statistical data, at each location, depending on the sampling rate, 16000 – 45000 image pairs are processed in this study. (For the convergence of the statistics, in the preliminary measurements, we compared the data from 3000 – 75000 image pares at $Re \simeq$8000. Then, although we confirmed that the convergence was seen with 30000 image pares for the clear channel region, we processed 45000 image pares. For the porous region, processing 16000 image pares was good enough.) The recorded data are processed by the Dynamics Studio 2015a software (DANTEC Dynamics) with the fast Fourier transform cross correlation technique. Each image is processed to produce instantaneous 101 $\times$ 74 vectors. When the ratio of the first and the second correlation peaks in an interrogation window is smaller than 1.3, it is removed from the process as an error vector. The moving-average validation proposed by Host-Madsen & McCluskey (1994), which evaluates each velocity vector comparing its neighbour vectors, is also applied with the acceptance factor of 0.1. The removed error vectors are approximately 3% and 5% of the total numbers processed for the clear flow and porous medium zones, respectively. The averaged number of pixels for a particle image captured by the CMOS camera in this study is confirmed to be more than 4 pixels. This indicates that the particle images are well resolved and the uncertainty in the measured displacement can be expected to be roughly less than 1/10th of the particle image diameter according to Prasad *et al.* (1992). Normalizing this uncertainty by the mean displacement length of the particles (Adrian *et al.* 2000) indicates that the estimated error in the magnitude of the instantaneous velocity is less than 4% of the maximum velocity in the measuring frame.

3. Results and discussions

3.1. *Mean velocity and secondary flows*

Figure 3 shows contour maps of the time- and streamwise-averaged streamwise velocity:

$$[\bar{u}]_x^f = \frac{\int_0^{4(D+d)} \bar{u} \mathrm{d}x^f}{\int_0^{4(D+d)} \mathrm{d}x^f}, \tag{3.1}$$

with the cross-sectional velocity vectors of case B at Re =3400 and 7700. (The vectors at $y/H = 0$ are produced by interpolating the values at planes $y4$ and $y5$.) Here, overbar denotes time averaging and $[\cdot]_x^f$ denotes fluid-phase averaging in the $x-$direction. The contour maps are painted with the $x - z$ plane measurement data while the vectors are produced using the $x - y$ and $x - z$ plane measurement data. Irrespective of the Reynolds number, it is seen that the cross-sectional secondary flow pattern is very different from the well known pattern in the square duct flow. A large single recirculation is seen near the upper corner and relatively weak recirculation can be seen near the porous interface while in a turbulent square duct flow (without a porous layer), the secondary flow consists of four pairs of counter-rotating vortices located at the duct corners. Accordingly, upward flows across the porous interface are observed in the middle region though their magnitudes are rather small. Due to the cross-sectional secondary flows, $[\bar{u}]_x^f$ shows skewed distribution near the top wall at $y/H = 1.0$. However, its distribution becomes much flatter near the porous interface at $y/H = 0.0$. These flow features verify the numerical simulation of Samanta *et al.* (2015) using the VANS equation for the porous region. Although Samanta *et al.* (2015) reported that the maximum magnitude of the secondary currents is approximately 8 % of the bulk velocity, which was four times as large as that of a regular duct of Vinuesa *et al.* (2014), the present results indicate approximately 6 % of the inlet velocity U_0. (The flow rates inside the porous layers are estimated as less than 5 % of the total flow rate by the mean velocity distribution discussed later. Hence, the difference between U_0 and the bulk velocity in the duct is in such an order.) It is considered that the magnitude difference of the secondary flows between the DNS and this study comes from the structural effects. Supporting this, our recent thermal field DNS (Kuwata *et al.* 2019) for the same flow geometry predicted the same order of the magnitude.

For the kinetic energy of the secondary flow $K_c = (\bar{u}^2 + \bar{v}^2)/2$, Vinuesa *et al.* (2018) discussed spanwise variations of its wall-normal averaged values: $[K_c]_y = (1/H)\int_0^H K_c \mathrm{d}y$, in several turbulent rectangular ducts. They reported that in turbulent square duct flows, the minimum $[K_c]_y$ was located near the symmetry plane and $[K_c]_y$ increased towards the side wall having a couple of local maxima. However, figure 4 indicates that for both the Reynolds numbers, $[K_c]_y$ tends to be larger towards the symmetry plane at $z/H = 0$ by the strong downward motions. Due to the centre of the large recirculation, which looks to be located near $z/H = 0.2$ (figure 3), $[K_c]_y$ has a local minimum there. Towards the side wall at $z/H = 0.5$, $[K_c]_y$ tends to rise again due to the energetic vertical motion along the side wall. For Re =7700, although a local kink is seen near $z/H = 0.065$–0.13, its reason is unclear. Since the number of the secondary flow data is $10(y) \times 7(z)$, it is not fine enough to capture local trends in detail, unfortunately. Since the magnitude of the present secondary flow velocity is significantly enhanced by the porous wall (three times larger than that in a square duct), the level of $[K_c]_y$ is approximately one order higher than those presented in Vinuesa *et al.* (2018). The magnitude level seems to be increased by the Reynolds number. Overall, in the porous duct flows, higher concentration of the energy appears near the symmetry plane as well as near the side wall for both the Reynolds numbers.

To see the effects of porous structures on the general flow fields, figure 5 compares the time- and streamwise-averaged vertical and streamwise velocity contour maps which are reconstructed using the $x - y$ plane measurement data. Although the structures of cases A and B are very different, irrespective of the Reynolds numbers, the mean velocity distributions in the clear duct region do not look very different from each other. For both the structures, strong downward velocity regions appear at $0.4 < y/H < 0.9$ near the symmetry planes of the clear ducts while strong upward velocity regions appear towards the top corners. Those distributions are consistent with the secondary currents (figure 3) and the trend of $[K_c]_y$ (figure 4). It is then suggested that the present structural difference does not significantly change the secondary flow patterns in the clear duct regions. As for the flows under the porous interfaces, case B shows stronger upward flows in the central regions than case A due to the structural difference.

3.2. *Sectional flow characteristics*

To show the examples of the detailed flow distributions inside the porous region, figures 6 and 7 show time-averaged streamwise velocity: $\bar{u}$, Reynolds shear stress: $-\overline{u'v'}$, and turbulent intensities (root mean square (RMS) velocities): u', v' in the symmetry planes of $z/H = 0$ at Re =7400 and 7700 for cases A and B, respectively. The position of $x/D = 0$ corresponds to the symmetry plane of the transverse rods shown in figure 2 (d). It is clear that depending on the porous structure, the profiles of the turbulence quantities change significantly. Due to the structures, the mean velocity shows apparent sinusoidal distribution profiles under the porous surfaces as seen in figures 6(a) and 7(a). However, when we focus on the penetration depth of the Reynolds shear stress shown in figures 6(b) and 7(b), which is assumed to be the length needed for the quantity to reach the asymptotic value under the interface, it is approximately equivalent to the rod height d. Indeed, the Reynolds shear stress is damped and almost vanishes up to $y = -d$. As for the RMS velocities, figure 7(c,d) indicates that the penetration lengths are much longer suggesting that turbulent fine eddies go deeply into the porous media depending on the porous structure. The budget term analysis for the turbulent flow over a permeable porous layer by Kuwata & Suga (2016*b*) found that the greater turbulence penetration towards the porous layer was due to the increased re-distribution and pressure diffusion processes intensified significantly by the pressure fluctuations. Hence, it is considered that the enhanced turbulent intensities under the porous layer are primarily due to the enhanced pressure fluctuations.

Figures 8 and 9 compare the sectional distributions of time- and streamwise-averaged quantities for cases A and B at Re =7400 and 7700, respectively. Among the seven planes, planes $z1$, $z4$ and $z6$ are plotted. For the streamwise mean velocity, it is clear that the distribution profiles are significantly skewed in the clear duct region of $y/H > 0$ as seen in figures 8(a) and 9(a). In both cases, the profiles look narrower in the symmetry plane (plane $z1$) than in the other planes. This trend is considered to be from the secondary currents and was also seen in Samanta *et al.* (2015). Due to the side walls, the secondary flow motions towards the duct corners enhance the flow rate around the duct corners leading to the flatter velocity profiles near the side walls. Although the maximum velocities in cases A and B are $1.3U_0$, the locations of the maximum velocities are at $y/H = 0.50$ and $y/H = 0.52$, respectively, which are slightly different from $y/H = 0.55$ by Samanta *et al.* (2015). Since the maximum values of the sinusoidal velocity profiles inside the porous layers are around $0.1U_0$, the flow rates inside the porous layers are estimated to be less than 5% of the inlet flow rates. It is clear that the mean velocities in both cases are significantly damped just under the porous surfaces and this trend is consistent with that observed in figures 6(a) and 7(a).

Corresponding to the mean velocities, the streamwise averaged Reynolds shear stresses of figures 8(b) and 9(b) show asymmetrical profiles in the clear duct region and are steeply damped just under the porous interfaces. As seen in figures 8(c,d) and 9(c,d), the streamwise averaged RMS velocity fluctuations show significantly different distribution profiles between cases A and B due to the structural difference. It is clear that although the streamwise RMS profiles steeply drop under the porous surfaces as the mean velocity and the shear stress profiles, the wall-normal RMS profiles do not show such a trend in both cases.

3.3. *Streamwise-spanwise plane-averaged flow characteristics*

As discussed with figure 3, although the flows are not two-dimensional over the porous surfaces, to see the general characteristics of porous medium flows, x–z plane averaging is applied by the trapezoidal rule using the x–y plane measurement data of planes $z1 - z5$ for $0 \leqslant z/H \leqslant 0.26$. Here, the x–z plane-averaged value is denoted as $[\cdot]_{xz}$. By this procedure, the control area (x–z plane) covers 4 ×1 unit-cells of the porous structure along the symmetry plane of the duct. From the time- and x–z plane-averaged (double-averaged) momentum equation (Whitaker 1996), the total momentum flux across the pores on the porous surface can be written as

$$\tau_p = \left(-\rho \left[\overline{u'v'}\right]^f_{xz} - \rho[\bar{u}]^f_{xz}[\bar{v}]^f_{xz} - \rho[\tilde{\bar{u}}\ \tilde{\bar{v}}]^f_{xz} + \mu \frac{\partial [\bar{u}]^f_{xz}}{\partial y} \right)_{y=0}, \tag{3.2}$$

where $[\tilde{\bar{u}}\ \tilde{\bar{v}}]^f_{xz}$ is the dispersion stress in which the dispersion of $\bar{u}_i$ is defined as $\tilde{\bar{u}}_i = \bar{u}_i - [\bar{u}_i]^f_{xz}$. Hence, by using the measured quantities, the friction velocity $u^p_\tau = \sqrt{\tau_p/\rho}$ on the porous surface can be obtained. Table 2 lists those friction velocities with the other parameters such as the permeability Reynolds numbers.

Figure 10 compares the plane-averaged streamwise mean velocity, Reynolds stress and RMS velocities at $Re \simeq$7500. For the velocity profiles in the clear flow region shown in figure 10(a), although there are slight discrepancies between the cases A and B, these two cases show nearly the same profiles. The shown DNS profile of Samanta *et al.* (2015) is for the symmetry plane and the Reynolds number is Re_b=5000. Also their porous structure is different from those of the present cases. Even with such differences, the present results well accord with the DNS data. The slip velocity U_w at the porous surface and δ_w, which is the location where the mean velocity has the maximum value, also do not significantly change in the two cases as listed in table 2. They are $U_w = 0.28U_0$ and $0.30U_0$ for cases A and B and $\delta_w = 0.52H$ for both cases. From the velocity profiles under the surface, although the sinusoidal profiles of cases A and B are different underneath the surface due to the structural difference, the general trends are similar to each other. When we define the penetration depth as the location to the first local minimum, it is clear that the penetration depths of the mean velocity of both cases are less than $y/H = 0.06$ which is the height d of the square rod constructing the porous media. Corresponding to the mean velocities, the shear stresses of both cases damp quickly until $y/H = 0.06$. Although some weak sinusoidal profiles are observed in the upper region of the porous layer, they eventually vanish deep inside the porous layer while the mean velocity does not show such a decay. Even though K_{yy} is 8.3 times larger in case B, the penetration depths of the mean velocity and the Reynolds shear stress do not seem to increase.

The trend that the flow variables look insensitive to the wall-normal permeability supports our previous conclusion in Suga *et al.* (2018) which suggested that although turbulence generation over porous media was enhanced by the permeable surface, it is rather insensitive to the wall-normal permeability K_{yy} compared with K_{xx} when $R_{yx} \geqslant 1.0$. We then suggested that flow was reasonably correlated to the permeability Reynolds number Re_{K_x} based on the streamwise permeability. Indeed, although K_{yy} of case B is 8.3 times larger than that of case A, the discrepancy between the two cases cannot be considered to reflect such large difference. Instead of the insensitivity to K_{yy}, Suga *et al.* (2018) showed that a 25 % increase of K_{xx} produced a certain amount of turbulence enhancement. While the penetrating fluids into the porous layer move towards the streamwise or spanwise direction, due to the large turbulent surface-shear, most of penetrating fluids move towards the streamwise direction. Since the penetration depths is not large, it is considered that the moving distances of the penetrating fluids in the streamwise direction are longer than those in the wall-normal direction. Hence, it is considered that among the wall-normal and streamwise permeabilities, the streamwise permeability affects more the turbulence near the porous surface. For the present data including the case at $R_{yx} = 0.8$ (case A), as seen in figure 10(*b*), case A whose K_{xx} is 19 % larger than that of case B shows 9.8% larger shear stress near the interface. Also, the profiles of the streamwise RMS velocities shown in figure 10(*c*) indicate that case A at $Re_{K_x} = 6.37$ is more turbulent than case B at $Re_{K_x} = 5.80$. Hence, the level of surface turbulence follows the order of Re_{K_x} even including the case of $R_{yx} < 1.0$

As for the RMS velocities in figure 10(*c*), although the plots of the DNS by Samanta *et al.* (2015) are for the symmetry plane and applied the averaged friction velocity over the whole porous surface, comparison is made to confirm the turbulence level. The corresponding streamwise permeability Reynolds numbers are Re_{K_x} =8.90, 6.37 and 5.80 for the DNS, cases A and B, respectively. Here, for the abscissa δ_w is the location of the maximum plane-averaged velocity. Although the levels of the present RMS results are in order of Re_{K_x}, the level of the DNS is somewhat lower than the present experiments even with the higher Re_{K_x}. Indeed, it is seen that although the levels of the RMS velocities by the DNS are similar to those of the present data, the peak value of the streamwise component and the levels of the RMS velocities in the porous layer are lower than the present experiments. Following Breugem *et al.* (2006), Samanta *et al.* (2015) assumed the permeability and the Forchheimer coefficient as $K_{\alpha\alpha} = d_p^2\varphi^3/[180(1-\varphi)^2]$

and $C^F_{\alpha\alpha} = \varphi d_p/[100(1-\varphi)]$, where d_p is the particle size for the loosely packed beds. In the DNS, $\varphi = 0.95$ and $d_p/H = 0.01$ were applied and these values produced the Forchheimer coefficient as $C^F_{\alpha\alpha}/H = 1.9 \times 10^{-3}$ while in the present cases $C^F_{\alpha\alpha}/H$ is in the range of $1.5\times10^{-4} - 6.6\times10^{-4}$ which is one order smaller than that of the DNS. Since the effect of a smaller $C^F_{\alpha\alpha}$ is comparable to that of a larger $K_{\alpha\alpha}$, it is considered that when the larger permeability enhances turbulence, the smaller Forchheimer coefficient also enhances turbulence. Note that in connection with equation (2.1), the drag force term in the momentum equation can be written as $f_i = \varphi\mu K^{-1}_{ij} \langle u_j\rangle^f + \varphi\mu K^{-1}_{ik} F_{kj} \langle u_j\rangle^f$. Hence, the Forchheimer tensor works similarly to the inverse of the permeability tensor in the double-averaged equation system. Also the larger Forchheimer coefficient and thus larger form drag caused the steep damping for the RMS velocities inside the porous layer for the DNS.

As far as the profiles inside porous layer are concerned, both cases A and B show very similar levels of the streamwise and wall-normal RMS velocities while some minor structural effects are seen. Unlike the shear stress profiles, both RMS velocities maintain certain levels and continue decaying inside the porous layer. Obviously the decaying rate is more gentle than those of the mean velocity and the shear stress. It is considered that although the shear generation is very weak, turbulent vortices penetrate against the upward secondary flow motion and dissipate at a deeper position inside the porous media. Particularly for the wall-normal direction, it is supposed that flow fluctuations are induced by the pressure fluctuations over the surface which propagate more deeply inside the porous media. These trends confirm the results reported by Breugem *et al.* (2006) who applied the volume averaged N-S equation for the porous medium region. Figure 10(*d*) compares the dispersion stresses $\left[\widetilde{\bar{u}}_i\widetilde{\bar{u}}_j\right]^f_{xz}$. It is obvious that the dispersion stresses are generally very small compared with the turbulent stresses. However, the streamwise component $\left[\widetilde{\bar{u}}\widetilde{\bar{u}}\right]^f_{xz}$ becomes comparable to the turbulent stress only in the region across the porous interface. This trend is consistent with that shown in Kuwata & Suga (2016*b*).

To see the trend of the RMS velocity more in details, to smooth the sinusoidal profiles, the square root values of the volume-averaged $\overline{u_i'^2}$:

$$\left\langle \overline{u_i'^2} \right\rangle^f = \frac{1}{4V^f_{REV}} \int_0^{(D+d)} \int_y^{y+D_{p_y}} \int_0^{4(D+d)} \overline{u_i'^2} \mathrm{d}v^f, \tag{3.3}$$

are plotted in figure 11 where V^f_{REV} is a representative elementary volume (REV) of the porous media defined as the fluid phase volume of $(D+d)\times D_{p_y} \times (D+d)$ in the homogeneous structure region. To the REV size in the y-direction $D_{p_y} = 4d$ is applied. Although case B has the structural interval of $2d$, the structural interval of case A is used for comparison. (Since for both cases the structures are homogeneous at $y < -d$, figure 11 shows the values under $y/D_{p_y} = -0.75$ which is the uppermost location of the REV centre.) For both the Reynolds numbers, although the streamwise component is dominant over the surfaces, the wall-normal component surpasses it below the surfaces and becomes dominant until $y/D_{p_y} \simeq -1.25$ and $y/D_{p_y} \simeq -1.5$ for cases A and B, respectively. Then, the streamwise component becomes dominant again and maintains the dominance deep inside the porous layer. This trend confirms that the wall-normal fluctuations penetrate more deeply than the streamwise ones while their decaying rate is higher suggesting that turbulence anisotropy is maintained inside the porous layer. The effects of the wall-normal permeability are not so significant to change the trend since the difference between the locations where the streamwise component surpasses the wall-normal component is rather small. The present trend of turbulence anisotropy at

$\varphi \simeq 0.8$ and at the range of $Re_{K_x} = 2.49 - 6.37$ is thus consistent with those observed in our previous DNS studies (Kuwata & Suga 2016*b*, 2017) which are for φ =0.7 – 0.84 at Re_K =3.8 – 6.1.

To confirm whether the mean velocity profiles near the symmetry plane are similar to those over two-dimensional porous wall flows, figure 12(a) shows the mean velocities over the porous surfaces in semi-logarithmic charts with fitting lines of the log-law:

$$[\bar{u}]^{p+}_{xz} = \frac{1}{\kappa} \ln \left(\frac{y + d_0}{h} \right). \tag{3.4}$$

This log-law form is usually applied to the flows over porous media and canopies (Best 1935; Nikora *et al.* 2002; Nepf & Ghisalberti 2008). Our previous report (Suga *et al.* 2018) showed that irrespective of anisotropy of the permeability, the von Kármán coefficient κ, the zero-plane displacement d_0 and the roughness scale h were generally well correlated with the pore-scale Reynolds number Re^{**}_K. The pore-scale Reynolds number was defined as

$$Re^{**}_K = \frac{u^p_\tau D_{p_x}}{3.8\nu}, \tag{3.5}$$

where D_{p_x} is the streamwise length of the pore. (Note that since this Reynolds number has a strong correlation with a permeability Reynolds number based on the porosity and the streamwise permeability, Suga *et al.* (2018) called it the “surrogate” permeability Reynolds number.) Table 2 lists the values of κ, $d^{p+}_0 (= u^p_\tau d_0/\nu)$ and $h^{p+} (= u^p_\tau h/\nu)$ which are obtained by the fitting procedure described in Breugem *et al.* (2006); Suga *et al.* (2010, 2017, 2018). The corresponding figure 12(b-d) shows that the present parameters are well in the clusters of the plots of a wide range of porous wall flows. This confirms that the turbulent flow over the porous surfaces near the symmetry plane of the square duct maintains the general trend of the mean velocity in the two-dimensional porous wall turbulence even though the secondary flows are enhanced. Note that for the von Kármán coefficient, the correlation with the pore-scale Reynolds number is not strong compared with the other parameters. Since the zero-plane displacement and the roughness scale are geometrical parameters related to the porous structure, the pore scale is reasonable parameter for the characteristic length scale. However, κy corresponds to the mixing length for near-wall turbulence and thus it is considered that the correlation between κ and the pore-scale is not very strong.

3.4. *Kelvin-Helmholtz instability waves*

Samanta *et al.* (2015) observed that there were short spanwise rollers in the middle region and their spanwise size was approximately $0.4H$. Following the discussion by Jiménez *et al.* (2001), those spanwise rollers are considered to be induced by the Kelvin-Helmholtz instability since the mean velocity has an inflection point under porous surface as seen in figure 10. Although Samanta *et al.* (2015) did not analyse the characteristics of those rollers, we try to detect and analyse the wave motions over porous media. Figure 13 shows one-dimensional spectrum of streamwise velocity fluctuations $E_{11,x}$ at $y/H = 0.1, 0.0$ and -0.02 in the symmetry planes. Those locations correspond to over, at and under the surface, respectively. For $Re \simeq 3500$, $y/H = 0.1$ and -0.02 correspond to $y^{p+} \simeq 30$ and -6, respectively, while for $Re \simeq 7500$, they correspond to $y^{p+} \simeq 75$ and -15, respectively. Both cases A and B at the surfaces ($y/H = 0$) show clear peaks. At $Re \simeq 3500$ shown in figure 13(a, b), the peaks of $y/H = 0.0$ locate at $f = 0.25$ Hz that corresponds to the wavelength of $\lambda_w = U_w/f = 1.4H$ due to the slippage velocity of $U_w = 0.28U_0$ as listed in table 2. At $Re \simeq 7500$ of case A, the peak of $y/H = 0.0$ locates at $f = 0.5$ Hz that corresponds to the wavelength of $\lambda_w = 1.8H$ while for case

B, it locates at $f = 0.6$ Hz that corresponds to the wavelength of $\lambda_w = 1.6H$ since U_w increases to $0.3U_0$. Accordingly, clear effects of the wall-normal permeability on the wavelengths are not observed also. Although the locations of the peaks of $y/H = -0.02$ slightly shift from those of $y/H = 0.0$, the corresponding frequencies are very similar to those of $y/H = 0.0$. This is because energy of the waves generated at the surfaces propagates to both over- and under-surface regions.

In the fully developed mixing layers, the normalized wavelength of the Kelvin-Helmholtz type coherent eddies by the vorticity thickness $C_\lambda = \lambda_x/\delta_\Omega$ is known to be $3.5 \leqslant C_\lambda \leqslant 5$ (Dimotakis & Brown 1976; Rogers & Moser 1994). For flows over porous walls, the DNSs by Breugem *et al.* (2006); Kuwata & Suga (2017) and the experiments by Suga *et al.* (2018) indicated $3.4 \leqslant C_\lambda \leqslant 5.5$ when the the boundary-layer thickness δ_w is considered to be equivalent to the vorticity thickness δ_Ω. The wavelength λ_w of cases A and B at $Re \simeq 3500$ produces $C_\lambda = \lambda_w/\delta_w$ =3.0 and 2.9, respectively. At $Re \simeq 7500$, for cases A and B they are C_λ =3.5 and 3.1, respectively. Although these values are close to the range of the reported values for the K-H waves, they are somewhat smaller than the reported values of turbulence over porous media. Although there are many unknown things regarding the interaction between the K-H instability and the side wall turbulent boundary layers, we believe that such interaction influences the instability resulting in the shorter wavelengths than those in two-dimensional boundary layer type of flows. This side wall confinement effect is stronger at the lower Reynolds numbers since the side wall boundary layer is thicker at the lower Reynolds number as seen in figure 3.

4. Conclusions

PIV measurements have been carried out for fully developed turbulent square duct flows over two transparent anisotropic porous media whose porosity is $\varphi \simeq$0.8 and ratios of the wall-normal to streamwise permeabilities are R_{yx} =0.8 and 7.8 at $Re \simeq$ 3500 and 7500. The corresponding streamwise permeability Reynolds numbers are Re_{K_x} =2.49 – 6.37 while the wall-normal permeability Reynolds numbers are Re_{K_y} =2.37 – 16.20. It is observed that irrespective of the porous structure, the well known four sets of counter rotating secondary flow patten in the square cross section changes to the flow pattern having one large recirculation near each solid corner accompanied with a weak counter rotation towards the porous corner. Although the porous structure is very different, this flow pattern is the same as that shown in the DNS of Samanta *et al.* (2015). The maximum magnitude of the secondary currents is approximately 6% of the inlet bulk velocity which is a little smaller than that of the DNS. It is confirmed that although turbulence is enhanced by the permeability, turbulence over and under the porous surface is rather insensitive to the wall-normal permeability compared with the streamwise component. Accordingly, Re_{K_x} is a better parameter that correlate to the porous wall turbulence at least $R_{yx} \geqslant 0.8$. It is also confirmed that the RMS velocities penetrate more deeply than the mean velocity and the wall-normal fluctuations need a longer distance to be damped in the porous media than the streamwise component. This suggests that although there is no shear generation, turbulent vortices penetrate against the upward secondary flow motion and dissipate at deeper locations inside porous media. It is considered that velocity fluctuations are drawn into the porous media by the pressure fluctuations over the surface which propagate more deeply inside the porous media. Accordingly, a little under the surface the wall-normal RMS velocity becomes larger than the streamwise component while the streamwise RMS velocity becomes dominant again deep inside the porous layer. However, interestingly the effect of the wall-normal permeability is also insignificant even for the penetration. For the streamwise-spanwise plane-averaged mean velocity near the symmetry plane, the correlations between the pore-scale Reynolds number and the log-law parameters such as the zero plane displacement, the von Kármán coefficient and the roughness scale are confirmed to be similar to those seen in a wide range of porous wall turbulence. The wavelengths of the spanwise rollers near the symmetry planes generated by a Kelvin-Helmholtz type instability are detected at the porous surfaces. While significant effects of the porous structure on the wavelengths are not observed, it is found that the wavelength tends to be shorter than those of porous walled channels possibly by the side wall effects while such a trend becomes weaker at higher Reynolds numbers. Overall, even with the enhanced secondary flows, near-porous-wall turbulence characteristics in the middle of the porous square duct are very similar to those of porous wall turbulent boundary layers while the side wall effects become apparent at low Reynolds numbers.

Acknowledgements

The authors express their gratitudes to their colleagues Messrs. Takanori Iida, Akira Taneo, Ryohei Okabe, Tomoya Matsuo, Kenya Igarashi and Dr. Masayuki Kaneda who assisted to perform the experiments. A part of this study was financially supported by the research grant (No. 24360073) of the JSPS.

Appendix A. Confirmation of the flow development

The position of the measuring section in this study is located at $X = 2.7$ m ($X/H = 54$) from the duct inlet. Here, X is the streamwise distance from the duct inlet. In the preliminary experiments, we measured flow quantities in the centre (symmetry) plane of the clear fluid region at several locations. Figure 14 compares turbulence quantities at X/H =38, 50 and 54 for $Re \simeq 8000$. It is seen that although the mean velocity profiles at three locations are almost the same, the Reynolds shear stress and the RMS velocities at $X/H = 38$ do not converge at the same levels of those at $X/H \geqslant 50$. It thus indicates that the flow is not fully developed yet at $X/H = 38$. Since there is no meaningful difference in the turbulence quantities at X/H =50 and 54, it can be said that the flow is fully developed at least by x/D =50. Therefore, it is confirmed that the presently measured flows are fully developed at the present measuring position at $X/H = 54$ for the cases at $Re \leqslant 8000$.

Declaration of interests

The authors declare that there is no conflict of interest.

REFERENCES

Abderrahaman-Elena, N. & García-Mayoral, R. 2017 Analysis of anisotropically permeable surfaces for turbulent drag reduction. *Phys. Rev. Fluids* **2**, 114609.

Adrian, R. J., Meinhart, C. D. & Tomkins, C. D. 2000 Vortex organization in the outer region of the turbulent boundary layer. *J. Fluid Mech.* **422**, 1–54.

Best, A. C. 1935 Transfer of heat and momentum in lowest layers of the atmosphere. *Tech. Rep.* 65. Geophys. Mem., Met. Off. Lond.

Breugem, W. P. & Boersma, B. J. 2005 Direct numerical simulations of turbulent flow over a permeable wall using a direct and a continuum approach. *Phys. Fluids* **17**, 025103.

Breugem, W. P., Boersma, B. J. & Uittenbogaard, R. E. 2006 The influence of wall permeability on turbulent channel flow. *J. Fluid Mech.* **562**, 35–72.

Dimotakis, P. E. & Brown, G. L. 1976 The mixing layer at high Reynolds number: large-structure dynamics and entrainment. *J. Fluid Mech.* **78**, 535–560.

Dunn, C., López, F. & García, M. 1996 Mean flow and turbulence in a laboratory channel with simulated vegetation. *Tech. Rep.* 51. Dept. Civil Eng., U.I.U.C., Illinois.

Host-Madsen, A. & McCluskey, D.R. 1994 On the accuracy and reliability of piv measurements. In *7th Int. Symp. Application of Laser Techniques to Fluid Mechanics*, pp. 214–226. Lisboa, Portugal.

Jiménez, J., Uhlmann, M., Pinelli, A. & Kawahara, G. 2001 Turbulent shear flow over active and passive porous surfaces. *J. Fluid Mech.* **442**, 89–117.

Kim, T., Blois, G., Best, J. L. & Christensen, K. T. 2018 Experimental study of turbulent flow over and within cubically packed walls of spheres: Effects of topography, permeability and wall thickness. *Int. J. Heat Fluid Flow* **73**, 16 – 29.

Kuwata, Y. & Suga, K. 2015 Progress in the extension of a second-moment closure for turbulent environmental flows. *Int. J. Heat Fluid Flow* **51**, 268–284.

Kuwata, Y. & Suga, K. 2016*a* Lattice Boltzmann direct numerical simulation of interface turbulence over porous and rough walls. *Int. J. Heat Fluid Flow* **61**, 145–157.

Kuwata, Y. & Suga, K. 2016*b* Transport mechanism of interface turbulence over porous and rough walls. *Flow Turb.Combust.* **97**, 1071–1093.

Kuwata, Y. & Suga, K. 2017 Direct numerical simulation of turbulence over anisotropic porous media. *J. Fluid Mech.* **831**, 41–71.

Kuwata, Y., Tsuda, K. & Suga, K. 2019 Direct numerical simulation of conjugate turbulent heat transfer in porous square duct. In *Proc. 11th Int. Symp. Turbulence and Shear Flow Phenomena*. Southampton, U. K.

Lovera, F. & Kennedy, J. F. 1969 Friction factors for flat bed flows in sand channels. *J. Hydr. Div., ASCE* **95**, 1227–1234.

Manes, C., Poggi, D. & Ridol, L 2011 Turbulent boundary layers over permeable walls: scaling and near-wall structure. *J. Fluid Mech.* **687**, 141–170.

Manes, C., Pokrajac, D., McEwan, I. & Nikora, V. 2009 Turbulence structure of open channel flows over permeable and impermeable beds: A comparative study. *Phys. Fluids* **21** (12), 125109.

Nepf, H. & Ghisalberti, M. 2008 Flow and transport in channels with submerged vegetation. *Acta Geophys.* **56**, 753–777.

Nezu, I. & Sanjou, M. 2008 Turburence structure and coherent motion in vegetated canopy open-channel flows. *J. Hydro-environ. Res.* **2**, 62 – 90.

Nikora, V., Koll, K., McLean, S., Dittrich, A. & Aberle, J. 2002 Zero-plane displacement for rough-bed open-channel flows. In *Int. Conf. Fluvial Hydraulics River Flow 2002*, pp. 83–92. Louvain-la-Neuve, Belgium.

Okazaki, Y., Kuwata, Y. & Suga, K. 2018 Comparison of turbulence over porous media with and without structural surface roughness. In *Proc. 12th Int. ERCOFTAC Symp. Engineering Turbulence Modelling and Measurements*. Montpelier, France.

Pokrajac, D. & Manes, C. 2009 Velocity measurements of a free-surface turbulent flow penetrating a porous medium composed of uniform-size spheres. *Transp. Porous, Med.* **78**, 367–383.

Prasad, A. K., Adrian, R. J., Landreth, C. C. & Offutt, P. W. 1992 Effect of resolution on the speed and accuracy of particle image velocimetry interrogation. *Exp. Fluids* **13**, 105–116.

Rogers, M. M. & Moser, R. D. 1994 Direct simulation of a self-similar turbulent mixing layer. *Phys. Fluids* **6**, 903–923.

Rosti, M. E., Brandt, L. & Pinelli, A. 2018 Turbulent channel flow over an anisotropic porous wall – drag increase and reduction. *J. Fluid Mech.* **842**, 381–394.

Ruff, J. F. & Gelhar, L. W. 1972 Turbulent shear flow in porous boundary. *J. Eng. Mech. Div., ASCE* **98**, 975–991.

Samanta, A., Vinuesa, R., Lashgari, I., Schlatter, P. & Brandt, L. 2015 Enhanced secondary motion of the turbulent flow through a porous square duct. *J. Fluid Mech.* **784**, 681–693.

Gómez-de Segura, G., Sharma, A. & García-Mayoral, R. 2018 Turbulent drag reduction using anisotropic permeable substrates. *Flow, Turb. Combust.* **100**, 995–1014.

SUGA, K. 2016 Understanding and modelling turbulence over and inside porous media. *Flow Turb. Combust.* **96**, 717–756.

SUGA, K., MATSUMURA, Y., ASHITAKA, Y., TOMINAGA, S. & KANEDA, M. 2010 Effects of wall permeability on turbulence. *Int. J. Heat Fluid Flow* **31**, 974–984.

SUGA, K., MORI, M. & KANEDA, M. 2011 Vortex structure of turbulence over permeable walls. *Int. J. Heat Fluid Flow* **32**, 586–595.

SUGA, K., NAKAGAWA, Y. & KANEDA, M. 2017 Spanwise turbulence structure over permeable walls. *J. Fluid Mech.* **822**, 186–201.

SUGA, K., NISHIMURA, W., YAMAMOTO, T. & KANEDA, M. 2014 Measurements of serpentine channel flow characteristics for a proton exchange membrane fuel cell. *Int. J. Hydrogen Energy* **39**, 5942–5954.

SUGA, K., OKAZAKI, Y., HO, U. & KUWATA, Y. 2018 Anisotropic wall permeability effects on turbulent channel flows. *J. Fluid Mech.* **855**, 983–1016.

VINUESA, R., NOORANI, A., LOZANO-DURÁN, A., KHOURY, G. K. EL, SCHLATTER, P., FISCHER, P. F. & NAGIB, H. M. 2014 Aspect ratio effects in turbulent duct flows studied through direct numerical simulation. *J. Turbul.* **15** (10), 677–706.

VINUESA, R., SCHLATTER, P. & NAGIB, H. M. 2018 Secondary flow in turbulent ducts with increasing aspect ratio. *Phys. Rev. Fluids* **3**, 054606.

WHITAKER, S. 1986 Flow in porous media I: A theoretical derivation of Darcy's law. *Transp. Porous Med.* **1**, 3–25.

WHITAKER, S. 1996 The Forchheimer equation: A theoretical development. *Transp. Porous Med.* **25**, 27–61.

ZAGNI, A. F. E. & SMITH, K. V. H. 1976 Channel flow over permeable beds of graded spheres. *J. Hydraul. Div.* **102**, 207–222.

ZIPPE, H. J. & GRAF, W. H. 1983 Turbulent boundary-layer flow over permeable and non-permeable rough surfaces. *J. Hydraul. Res.* **21**, 51–65.

Porous med.	φ	R_{yx}	$K_{xx}(\mathrm{mm}^2)$	$K_{yy}(\mathrm{mm}^2)$	$K_{zz}(\mathrm{mm}^2)$	$C^F_{xx}(\mathrm{mm})$	$C^F_{yy}(\mathrm{mm})$	$C^F_{zz}(\mathrm{mm})$
case A	0.77	0.8	0.19	0.15	0.19	0.0075	0.014	0.0075
case B	0.75	7.8	0.16	1.25	0.16	0.0096	0.033	0.0096

TABLE 1. Characteristics of porous media; the porosity φ is calculated from the porous structure; the diagonal components of the permeability tensor $K_{\alpha\alpha}$ and the coefficient of the Forchheimer tensor $C^F_{\alpha\alpha}$ are measured values; $R_{yx} = K_{yy}/K_{xx}$.

Porous med.	Re	Re_{K_x}	Re_{K_y}	Re^{**}_K	u^p_τ/U_0	δ_w/H	U_w/U_0	κ	d^{p+}_0	h^{p+}	$x-y$	$x-z$
case A	3300	2.67	2.37	16.1	0.095	0.47	0.28	0.16	55	20	✓	
	7400	6.37	5.66	38.5	0.102	0.52	0.28	0.16	172	70	✓	
case B	3400	2.49	6.97	16.4	0.094	0.49	0.30	0.16	40	18	✓	✓
	7700	5.80	16.20	38.1	0.097	0.52	0.30	0.16	115	52	✓	✓

TABLE 2. Experimental conditions and measured parameters of the mean velocity fields; Re, Re_{K_x}, Re_{K_y} and Re^{**}_K are the Reynolds number based on the inlet velocity U_0, the permeability Reynolds numbers based on $\sqrt{K_{xx}}$, $\sqrt{K_{yy}}$ and the pore scale Reynolds number defined by equation (3.5); u^p_τ is the friction velocity over the porous wall calculated with the streamwise-spanwise plane-averaged values by equation (3.2); the boundary layer thickness δ_w and the slip velocity U_w are from the plane-averaged mean velocity; κ, d_0 and h are the von Kármán coefficient, the zero plane displacement and the roughness scale, respectively; $(\cdot)^{p+}$ corresponds to a value normalized by using u^p_τ.

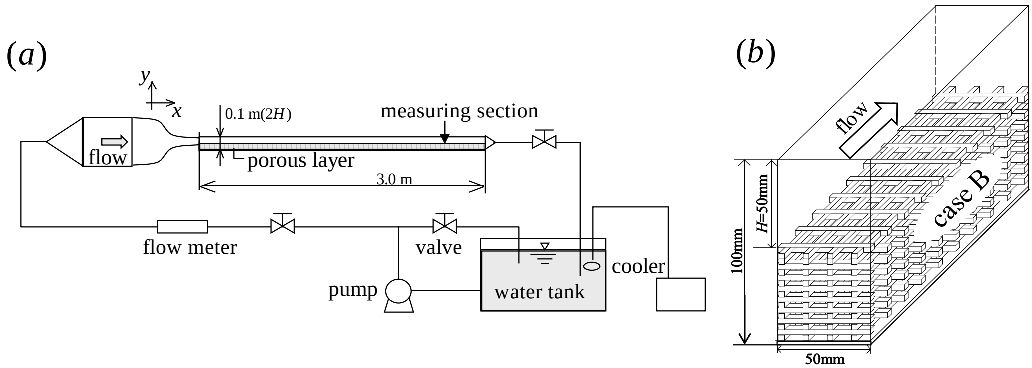

FIGURE 1. Experimental setup; (*a*) flow facility, (*b*) test section.

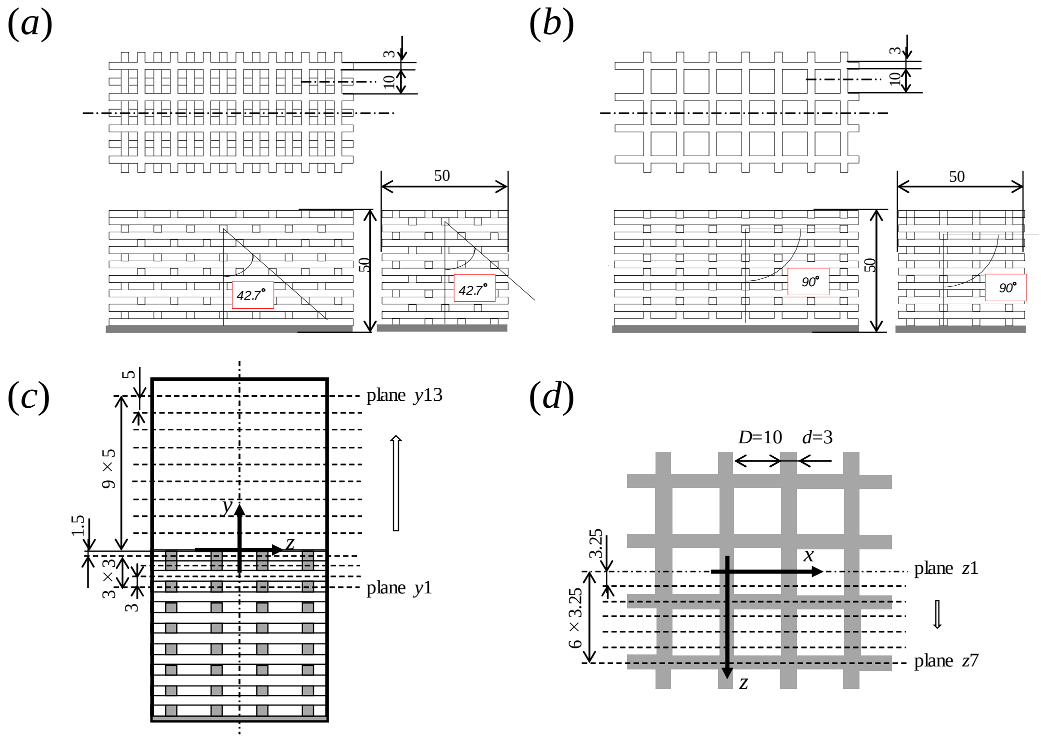

FIGURE 2. Structures of porous media, measuring sections and definition of the coordinates: (*a*) case A, (*b*) case B, (*c*) measurement planes of $x - z$ plane measurements, (*d*) measurement planes of $x - y$ plane measurements.

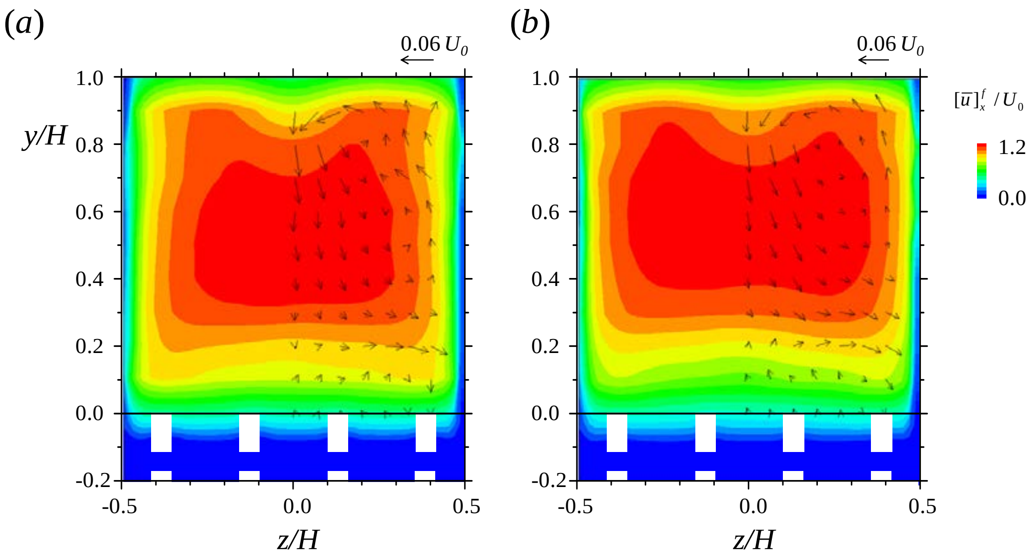

FIGURE 3. Cross sectional mean velocity and secondary flows of case B: (a) at $Re = 3400$, (b) at $Re = 7700$.

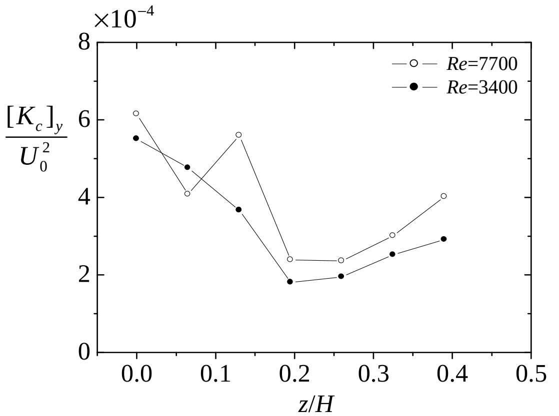

FIGURE 4. Spanwise variation of the kinetic energy of the secondary flow averaged over the wall-normal direction in case B.

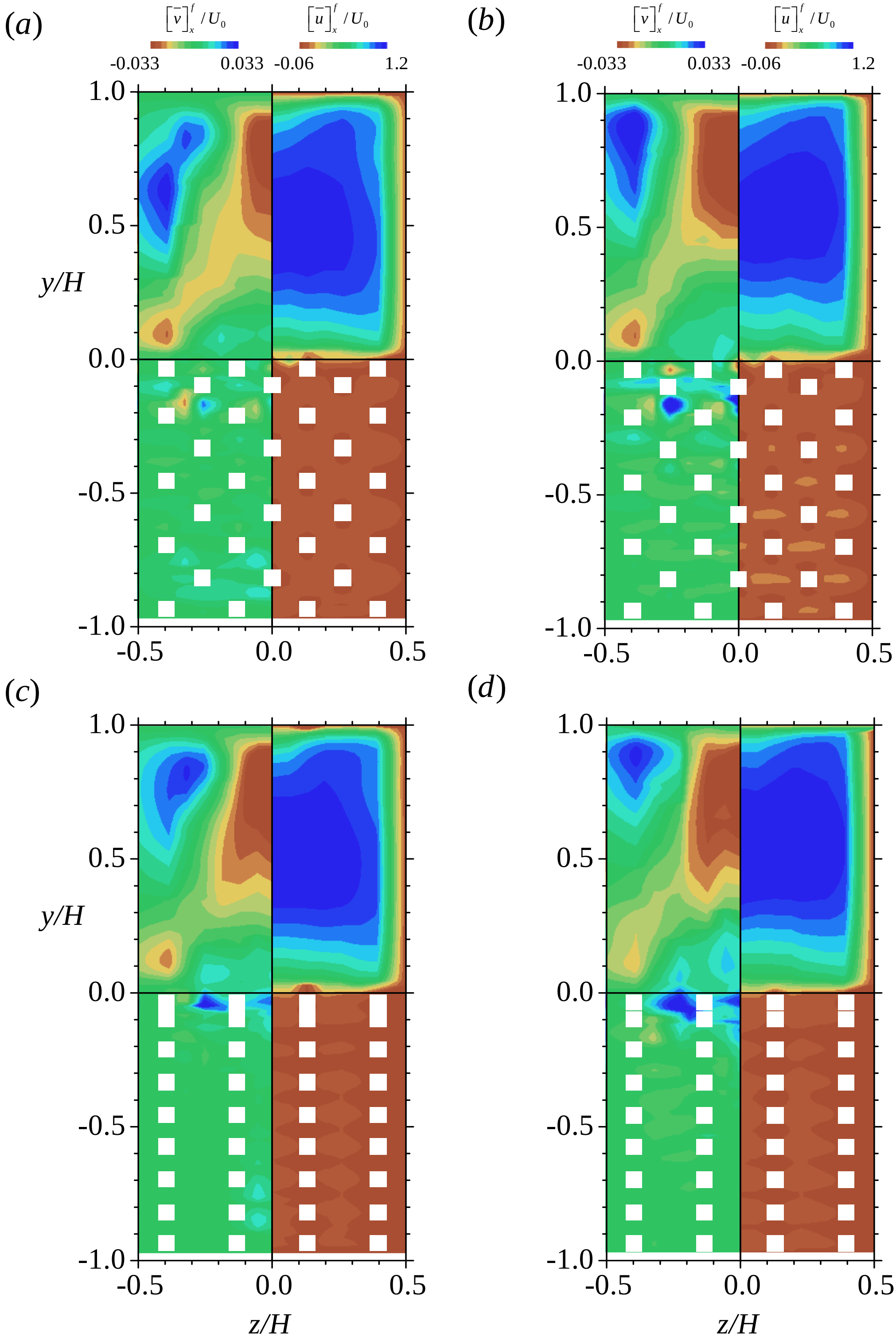

FIGURE 5. Cross sectional mean velocity contour maps: (a) case A at $Re = 3300$, (b) case A at $Re = 7400$, (c) case B at $Re = 3400$, (d) case B at $Re = 7700$. The z/H location for $[\overline{v}]^f_x$ is reversed for presentation.

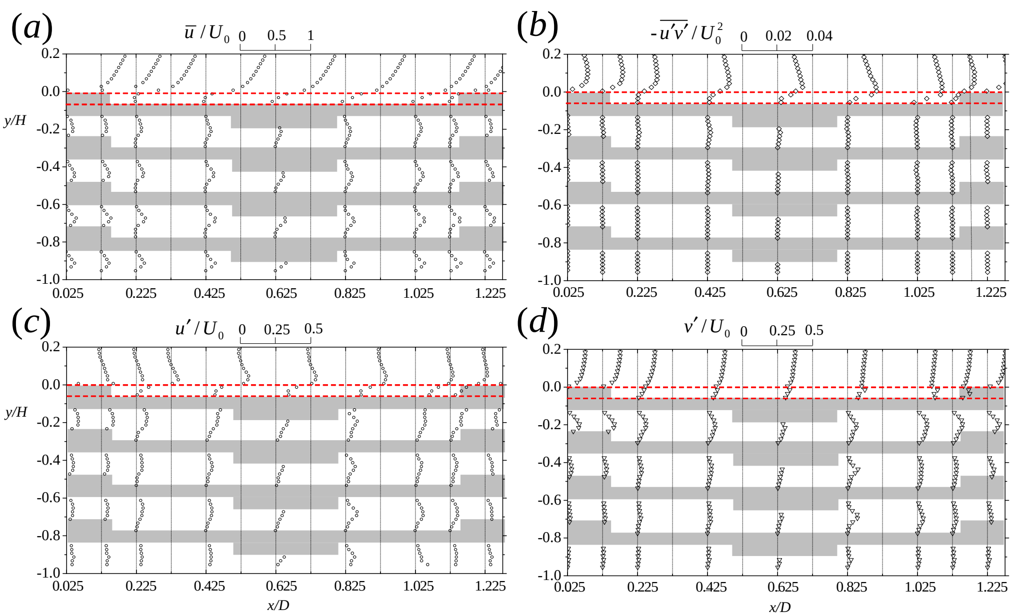

FIGURE 6. Time-averaged turbulence quantities in the symmetry plane (plane $z1$ at $z/H = 0$) in case A at $Re = 7400$: (a) streamwise velocity, (b) Reynolds shear stress, (c) streamwise RMS velocity, (d) wall-normal RMS velocity. Red broken lines show positions at $y = 0$ and $y = -d$.

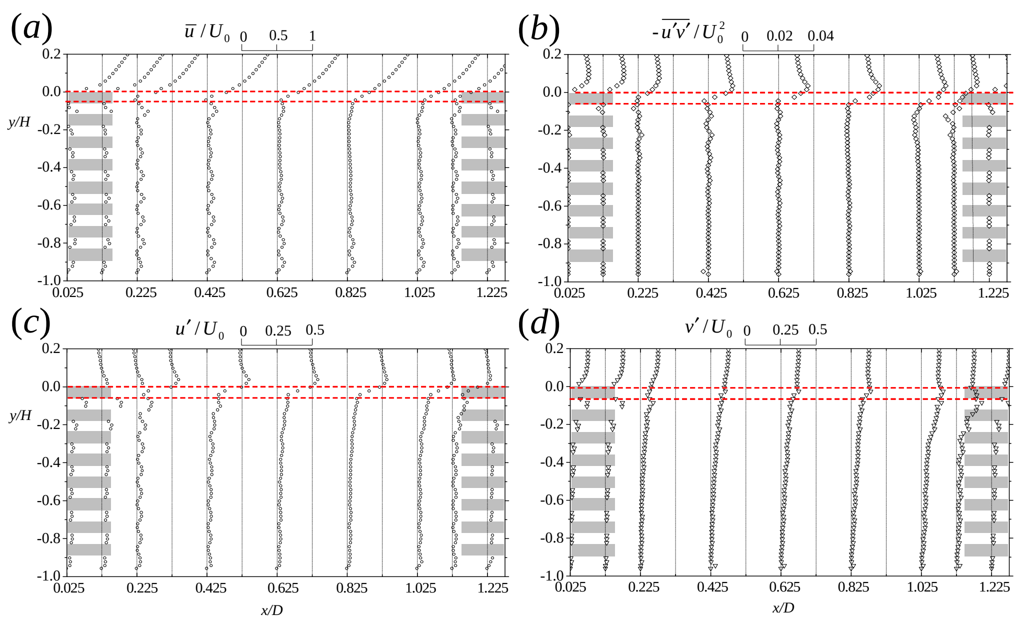

FIGURE 7. Time-averaged turbulence quantities in the symmetry plane (plane $z1$ at $z/H = 0$) in case B at $Re = 7700$: (a) streamwise velocity, (b) Reynolds shear stress,(c) streamwise RMS velocity, (d) wall-normal RMS velocity. Red broken lines show positions at $y = 0$ and $y = -d$.

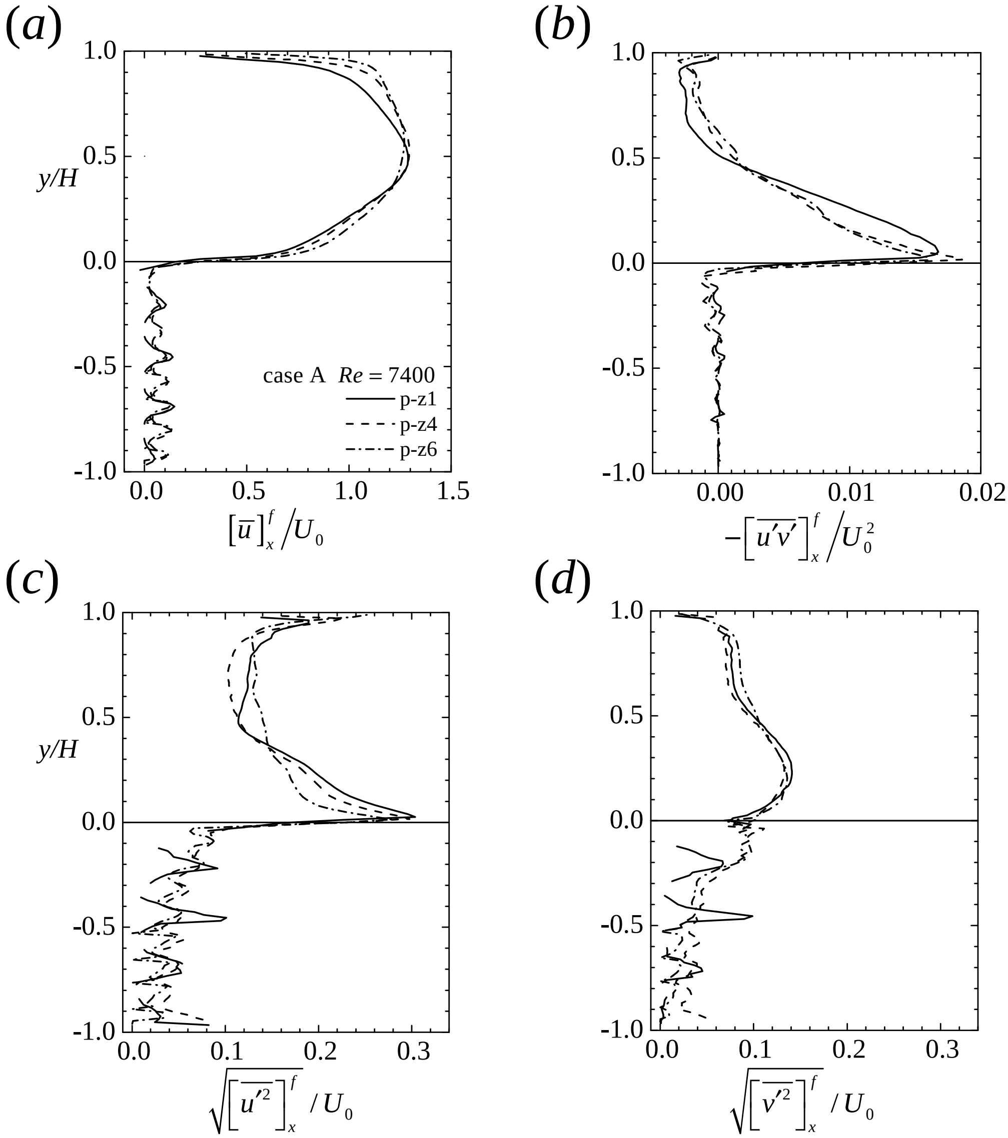

FIGURE 8. Distributions of streamwise-averaged turbulence quantities of case A at $Re = 7400$: (a) streamwise velocity, (b) Reynolds shear stress, (c) streamwise RMS velocity, (d) wall-normal RMS velocity.

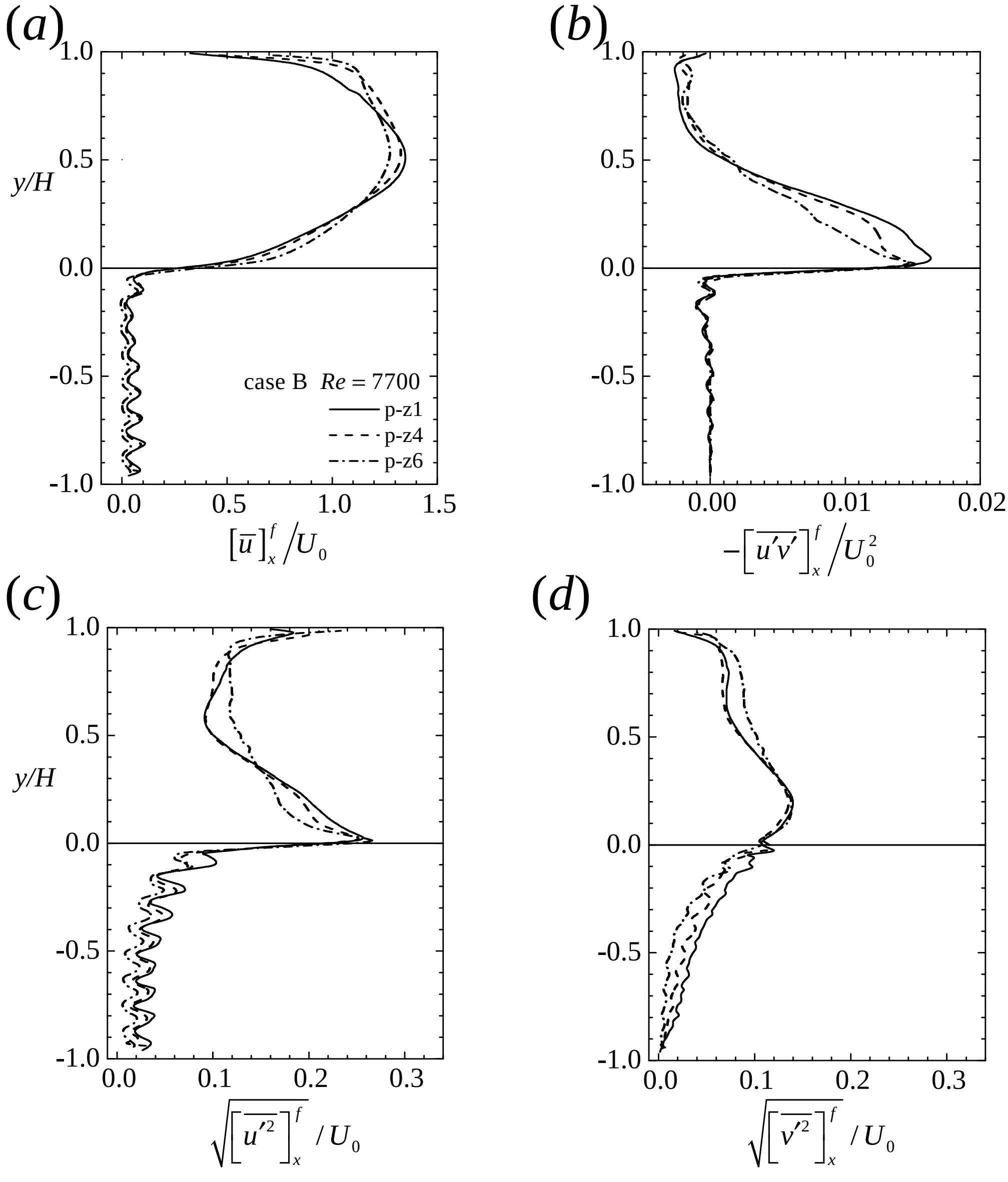

FIGURE 9. Distributions of streamwise-averaged turbulence quantities of case B at $Re = 7700$: (a) streamwise velocity, (b) Reynolds shear stress, (c) streamwise RMS velocity, (d) wall-normal RMS velocity.

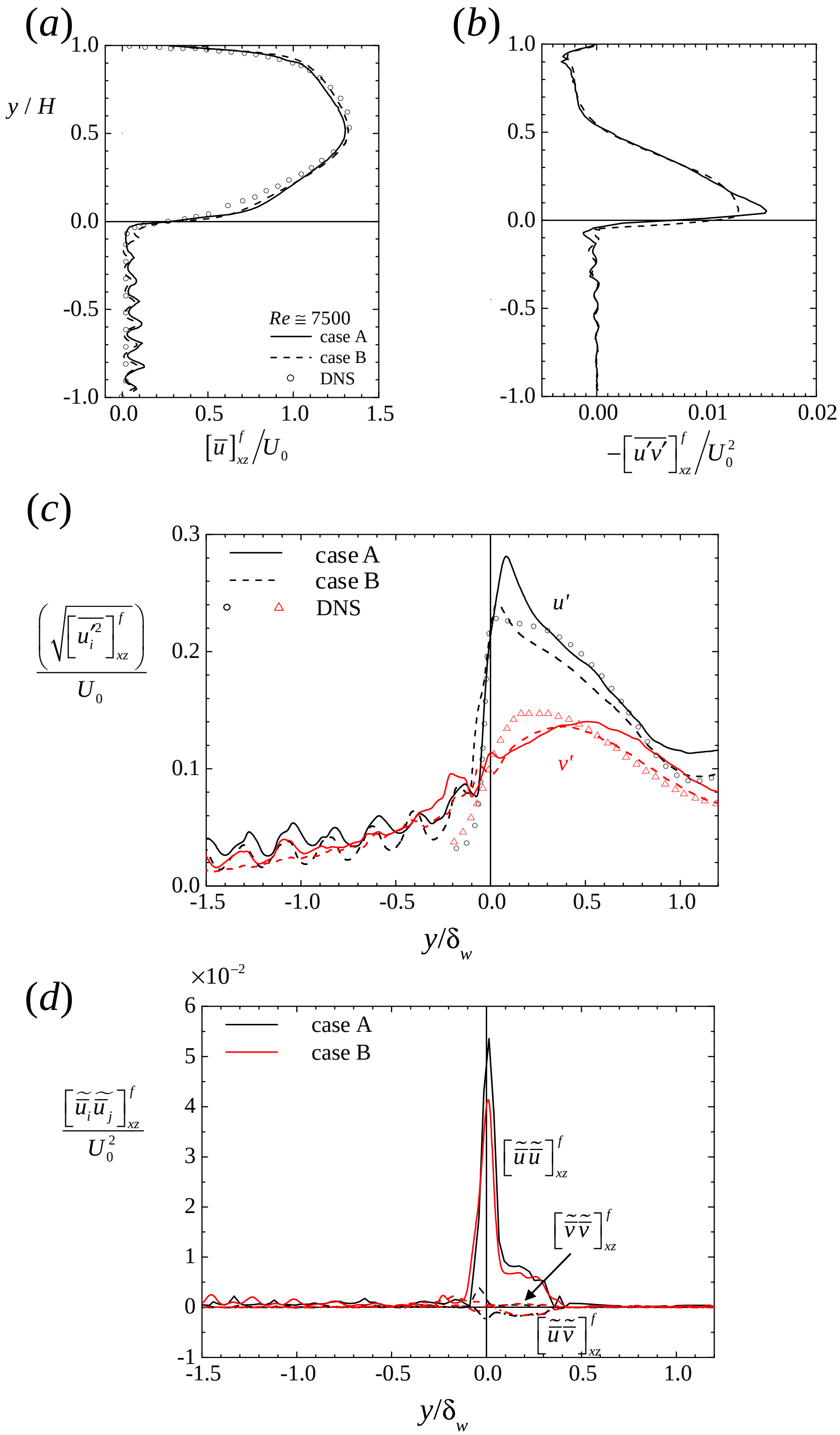

FIGURE 10. Comparison of plane-averaged turbulence quantities at $Re \simeq 7500$ (at Re = 7400 for case A; at Re = 7700 for case B): (*a*) streamwise velocity, (*b*) Reynolds shear stress, (*c*) streamwise and wall-normal RMS velocities, (*d*) dispersion stresses. The DNS data (Samanta *et al.* 2015) are at Re_b=5000 in the symmetry plane.

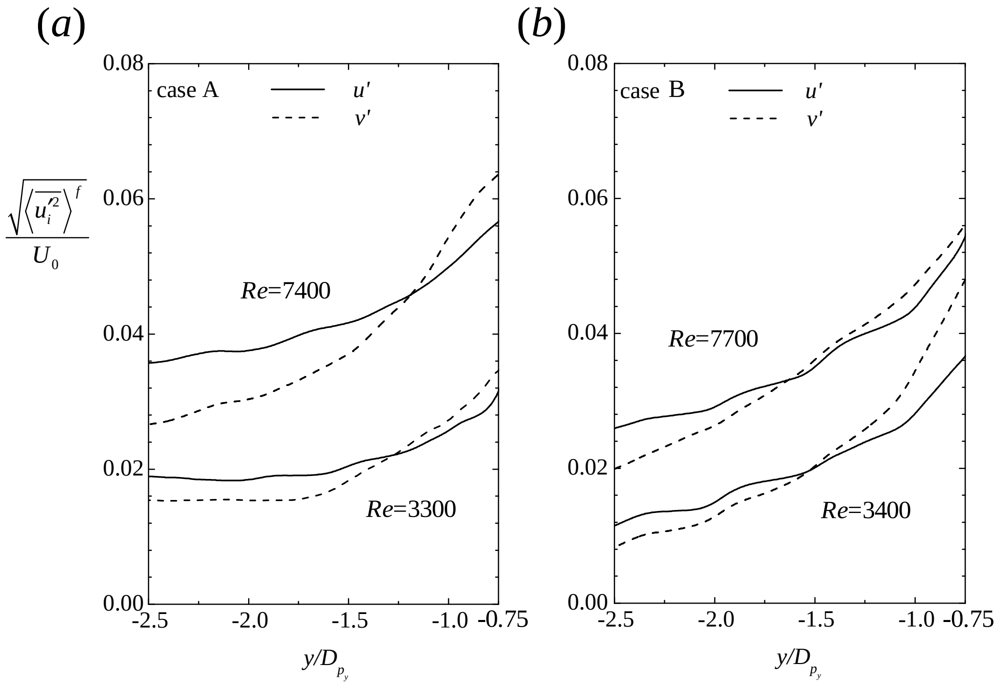

FIGURE 11. RMS velocities by the REV averaging: (a) case A, (b) case B. $D_{p_y} = 4d$.

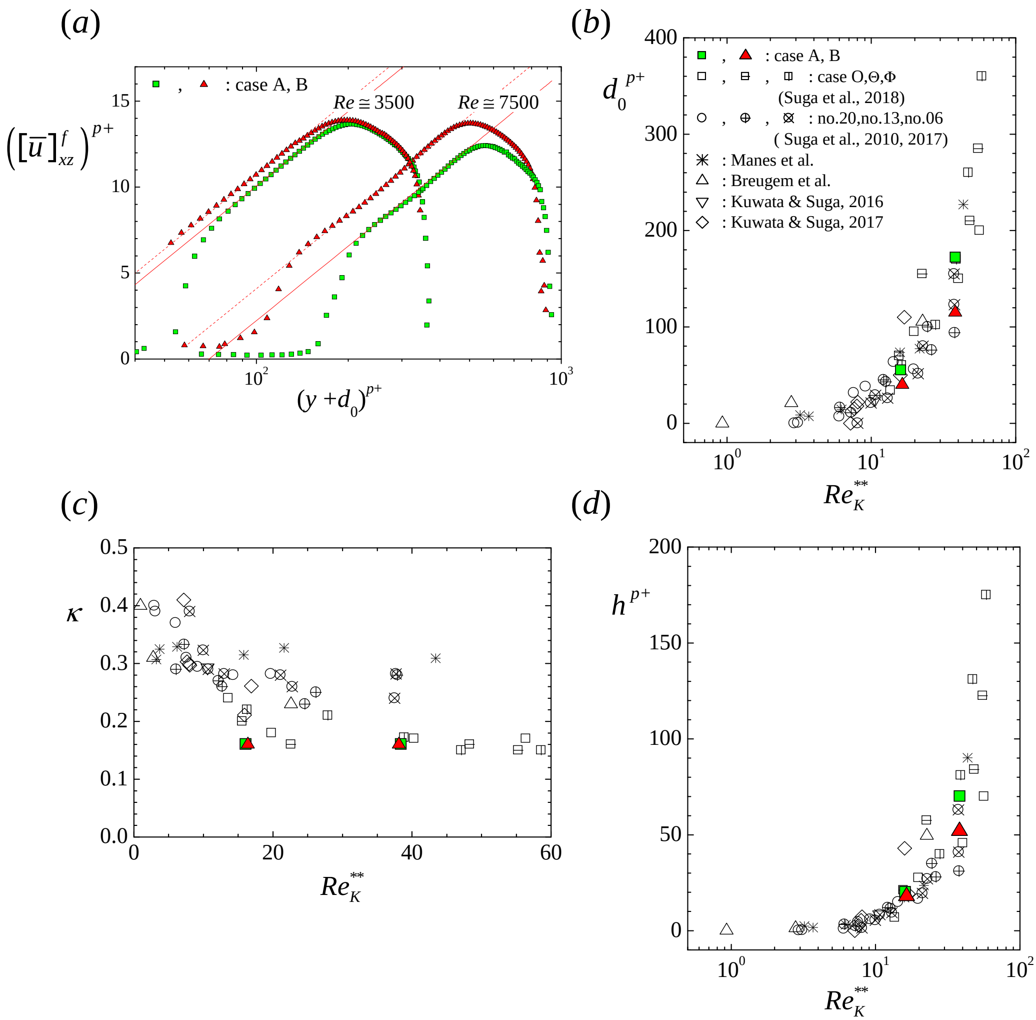

FIGURE 12. Distributions of the mean velocities and log-law parameters against the pore-scale Reynolds number: (*a*) streamwise mean velocity distributions in semi-log scale, (*b*) zero-plane displacement, (*c*) von Kármán coefficient, and (*d*) roughness scale. The red lines in (*a*) are fitting lines. Data of Suga *et al.* (2010, 2017); Manes *et al.* (2011); Breugem *et al.* (2006); Kuwata & Suga (2016*a*) are for isotropic porous media while data of Kuwata & Suga (2017); Suga *et al.* (2018) are for anisotropic porous media.

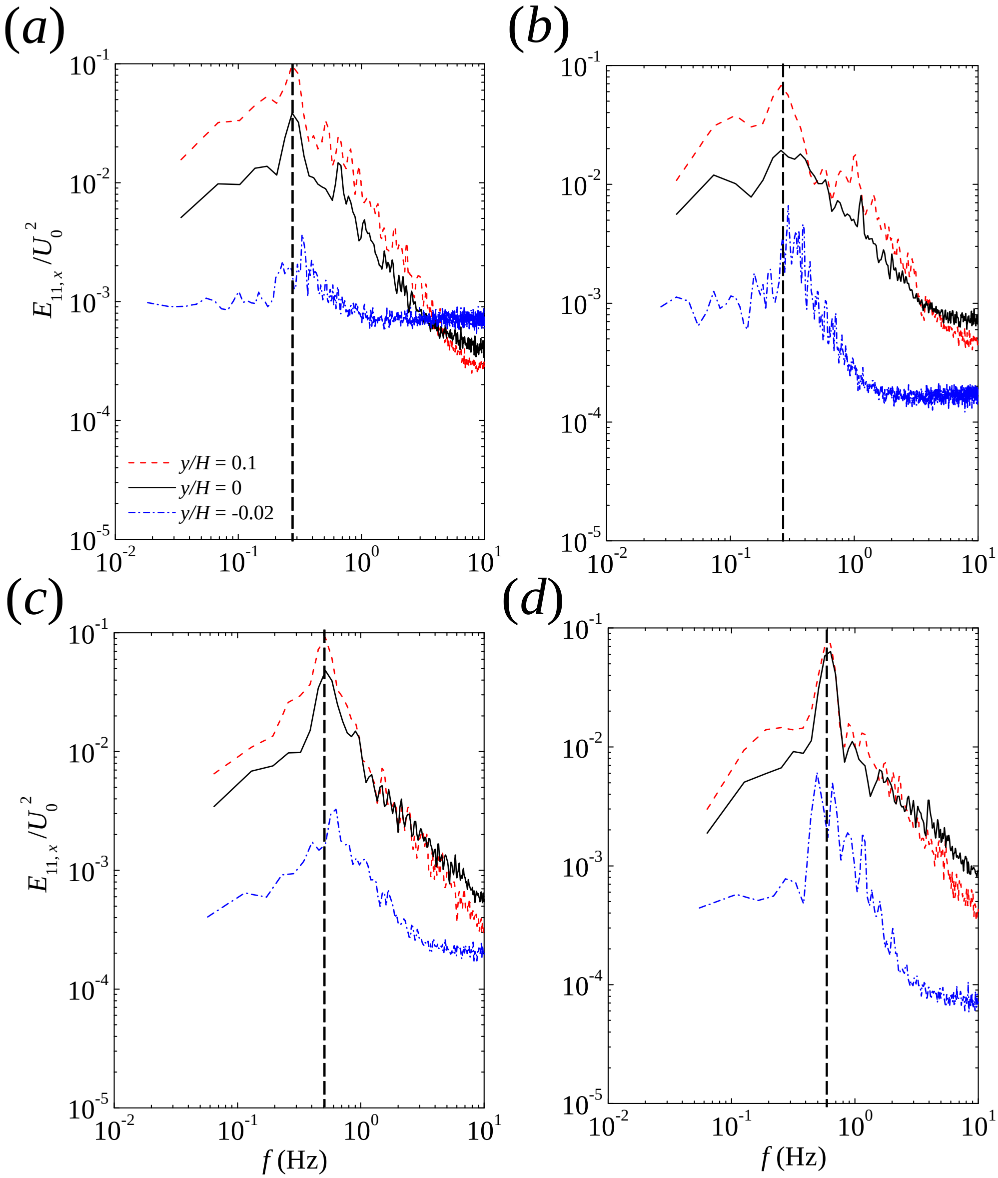

FIGURE 13. One-dimensional streamwise spectrum of u' in the symmetry plane: (a) case A at $Re = 3300$, (b) case B at $Re = 3400$, (c) case A at $Re = 7400$, (d) case B at $Re = 7700$. Black broken lines correspond to the frequencies of peak locations at the surface: $y/H = 0.0$.

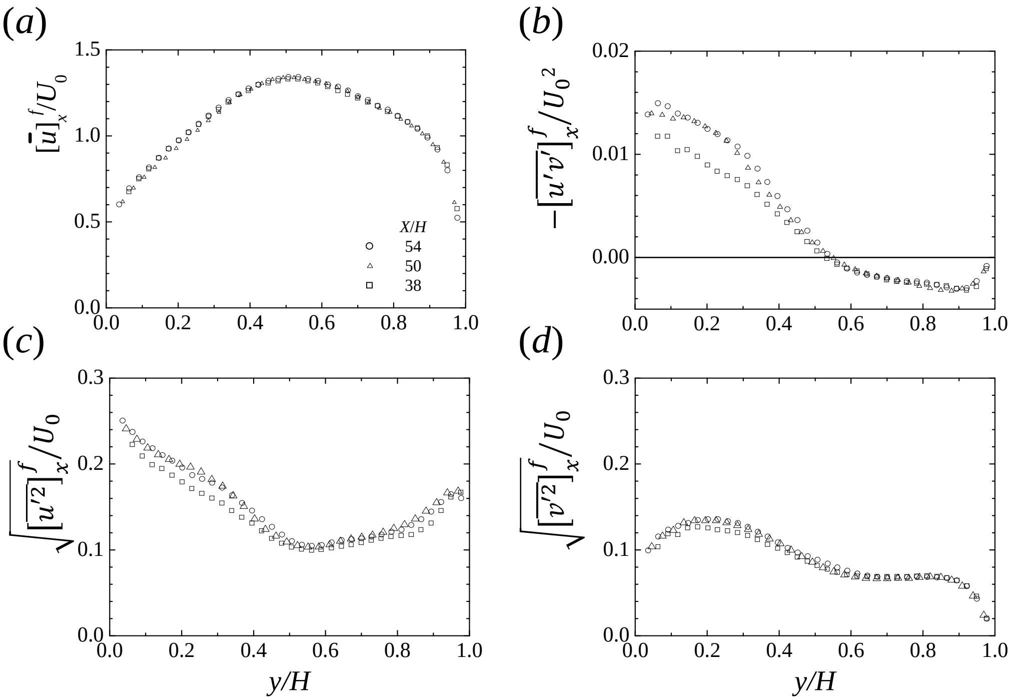

FIGURE 14. Comparison of the centre plane turbulence quantities of case B at $Re \simeq 8000$: (*a*) mean velocity, (*b*) Reynolds shear stress, (*c*) streamwise RMS velocity, (*d*) wall-normal RMS velocity.